The Astronomical Journal, 128:1541–1551, 2004 October

HUBBLE SPACE TELESCOPE SPECTROSCOPY OF FOUR LUMINOUS COMPACT BLUE GALAXIES AT INTERMEDIATE REDSHIFT[1]

C. Hoyos,[2] R. Guzmán,[3] M. A. Bershady,[4] D. C. Koo,[5] and A. I. Díaz[2]

Received 2003 September 22; accepted 2004 June 29

ABSTRACT

We present a spectroscopic study of four blue ($B - V \leq 0.6$) compact ($\mu_B \leq 21.0$ mag arcsec^{-2}) field galaxies with redshifts $0.095 \leq z \leq 0.438$ and absolute magnitudes M_B between -17.5 and -21.1. The spectra, taken with the Space Telescope Imaging Spectrograph on board the *Hubble Space Telescope*, show prominent emission lines whose spatial profiles reveal, at least in two cases, the existence of various star-forming regions and an underlying stellar population. The derived star formation rates from Hα luminosities in these star-forming regions range between 0.5 and 7 $M_\odot$ yr^{-1}. These regions are typically 10 times more luminous than and approximately twice as large as the well-known giant H II region 30 Doradus in the LMC. When compared with local starburst galaxies, the objects presented here turn out to be very similar to the brightest H II galaxies in terms of the areal star formation rate and in the ratio between the galactic half-light diameter to the line-emitting region half-light diameter ($D_{\rm eff}/D_0$).

Key words: galaxies: evolution — galaxies: ISM — galaxies: starburst

1. INTRODUCTION

Blue compact galaxies (BCGs) were first identified by Zwicky (1965) as faint starlike field galaxies on Palomar Sky Survey plates. BCGs often present an emission-line spectrum and a UV excess.

The *Hubble Space Telescope* (*HST*) has provided a great deal of information about the nature of these faint BCGs. Such galaxies include low-luminosity dwarfs at low redshift (Im et al. 1995), starburst galaxies (Cowie et al. 1991), and low-luminosity active galactic nuclei at $z \leq 1$ (Tresse et al. 1996). Faint BCGs also include the so-called compact narrow emission-line galaxies (CNELGs; Koo et al. 1994, 1995; Guzmán et al. 1996).

In Jangren et al. (2004) the name luminous compact blue galaxies (LCBGs) was assigned to those luminous ($M_B < -17.5$), compact ($\mu_B \leq 21.0$ mag arcsec^{-2}), and blue ($B - V \leq 0.6$) galaxies undergoing a major starburst. This definition is meant to include the most luminous local BCGs, as well as various families of starbursts at intermediate z. An important feature of our sample selection is that this population of generally isolated, high surface brightness objects can be observed over a wide redshift range. For instance, Lyman break galaxies (Lowenthal et al. 1997; Pettini et al. 1998) at $z > 2$ would be among the brightest LCBGs, according to this definition. LCBGs are thought to contribute up to $\sim$50% of the star formation rate density in the universe at $z \approx 1$, and they are the most rapidly evolving population responsible for the observed evolution of the luminosity function (Lilly et al. 1995). They are therefore of great relevance for the study of the star formation rate in the universe and a key to our understanding of the evolution of galaxies at cosmic scales.

Their relation to local populations, however, is not well understood. A detailed study of 45 such objects can be found in Guzmán et al. (1997) and Phillips et al. (1997). This population of LCBGs is far from constituting a homogeneous class of objects: around 60% of them are "H II–like" objects, whereas the rest are classified as "starburst disklike." H II galaxies are a subset of BCGs in which the spectrum is completely dominated by a component, present almost everywhere within the galaxy, that resembles the emission of an H II region (Sargent & Searle 1970). Starburst nuclei were introduced in Balzano (1983); they show high extinction values, with very low [N II] λ6584/Hα ratios and faint [O III] λ5007 emission. Their Hα luminosities are always greater than 10^8 $L_\odot$.

In order to investigate further the nature of LCBGs at intermediate redshift and identify their local counterparts, we have studied the sizes and the areal star formation of the star-forming regions in LCBGs. The half-light radius of both the line-emitting region and the host galaxy can be used to parametrize the size of the starburst relative to the underlying population, while the star formation rate per unit area and galactic mass are used to rank the intensity of the star-forming episode.

In this paper we present two-dimensional spectra of four LCBGs with redshifts between 0.095 and 0.438 that were obtained with the Space Telescope Imaging Spectrograph (STIS) on the *HST*. These objects were originally classified as CNELGs in Koo et al. (1994). They were selected as stellar-like objects with colors unlike typical stars in *UBV* two-color diagrams. Two of the galaxies presented here were observed with *HST*/WFC (Koo et al. 1994), and the other two were observed with the *HST*/WFPC2 (Guzmán et al. 1998). Spectroscopic works dealing with these objects can be found in Guzmán et al. (1996) and Koo et al. (1995). The selected sources are in the fields SA68, SA57, and HER1 and were selected to span a wide range in luminosity ($-21.1 \leq M_B \leq -17.5$).

[1] Based on observations obtained with the NASA/ESA *Hubble Space Telescope* obtained at the Space Telescope Science Institute, which is operated by the Association of Universities for Research in Astronomy, Inc., under NASA contract NAS5-26555.

[2] Departamento de Física Teórica, Modulo C-XI, Facultad de Ciencias, Universidad Autónoma de Madrid, Cantoblanco, E-28049 Madrid, Spain; carlos.hoyos@uam.es, angeles.diaz@uam.es.

[3] Bryant Space Science Center, University of Florida, Gainesville, FL 32611-2055; guzman@astro.ufl.edu.

[4] Department of Astronomy, University of Wisconsin, 475 North Charter Street, Madison, WI 53706; mab@astro.wisc.edu.

[5] Department of Astronomy, University of California, Santa Cruz, CA 95064; koo@ucolick.org.

TABLE 1
LOG OF *HST*/STIS SPECTROSCOPY

	H1-13088	SA57-10601	SA68-6134	H1-13385
Object ID	1	2	3	4
R.A. (J2000.0)	17 20 19.67	13 08 47.8	00 18 11.34	17 21 15.72
Decl. (J2000.0)	50 01 04.7	29 23 41.1	15 47 52.8	50 01 38.0
Observation Date	2000 Nov 06	2000 Jul 05	2001 Oct 20	2001 Aug 10
Total Exposure Time (s)	4932	4696	4656	4932
z	0.436	0.438	0.285	0.095
$t_{\rm lookback}$ (Gyr)	3.9	3.9	2.9	1.2
M_B	−21.1	−20.4	−19.8	−17.5
R_e (kpc)[a]	2.7	2.1	1.0	0.69
m_B	21.0	21.6	21.4	20.9
r_e (arcsec)[a]	0.47	0.36	0.23	0.39

NOTE.—All quantities given were calculated assuming $q_0 = -0.55$ and $H_0 = 70$ km s^{-1} Mpc^{-1}. Units of right ascension are hours, minutes, and seconds, and units of declination are degrees, arcminutes, and arcseconds.
[a] Half-light radii.

The *HST* spatially resolved spectroscopy can help us constrain better the nature of these LCBGs by providing

1. The distribution of the stellar component and the nebular component within these galaxies, as it yields a measure of the size of the star-forming region relative to the galaxy as a whole. The fraction of the galaxy involved in the star-forming event is also of importance, since the amount of fading depends on it.
2. The star formation rate per unit area, which yields a measurement of the intensity of the star-forming episode and of the star formation efficiency as well.
3. Well-resolved rotation curves. This would give a direct determination of the mass enclosed within the line-emitting region. This kinematic study will be presented in a follow-up paper (Bershady et al. 2004).

Section 2 of this paper describes the details of the observations, data reduction, and involved errors and uncertainties. The analysis of the structure and the star formation properties of the star-forming regions are presented in § 3. The summary is § 4.

The cosmology assumed here is a flat universe with $\Omega_\Lambda = 0.7$ and $\Omega_m = 0.3$. The resulting cosmological parameters are $H_0 = 70$ km s^{-1} Mpc^{-1} and $q_0 = -0.55$. Given these values, $1''$ corresponds to 1.8 kpc at $z = 0.1$ and to 5.8 kpc at $z = 0.45$.

2. OBSERVATIONS AND DATA REDUCTION

Target names, redshifts, look-back times, B absolute magnitudes, and half-light radii, as well as an identifying number for the observed objects, are given in Table 1.

The spectra were obtained using the STIS instrument on board *HST*. The detector used was the STIS CCD, a SITe 1024×1024 chip, with $0''.05$ square pixels operating from ~2000 to 11000 Å.

The instrumental configuration used was a low-resolution grating, G750L, providing a dispersion of 4.92 Å pixel^{-1}, or about 190 km s^{-1} pixel^{-1}, which, in combination with a slit $0''.5$ wide, gives a spectral resolution of about 29 Å (FWHM). The spectral coverage provided by this setup is about 5000 Å. The central wavelength is 7750 Å. For each target, two different observation sets, each one consisting of two different exposures, were carried out. The exposure time for each single exposure is around 1200 s. Total exposure times for each object are listed in Table 1. The spectra allowed us to measure emission-line fluxes for [O II] λ3727, Hβ, [O III] $\lambda\lambda$4959, 5007, Hα and, for one object, [S II] $\lambda\lambda$6717, 6731. The spectra were not dithered along the slit.

The higher resolution grating G750M was also used. It provides a dispersion of 0.53 Å pixel^{-1}, or about 35 km s^{-1} pixel^{-1}. The slit width used was $0''.2$, thus giving a spectral resolution of about 0.9 Å (FWHM). The spectral coverage provided by this setup is about 500 Å. The results from this data will be presented in a later paper (Bershady et al. 2004).

The data were reduced using the STSDAS[6] package within IRAF.[7] Reduction steps follow standard procedures: bias subtraction, cosmic-ray rejection within one data set, dark-current removal, flat fielding, wavelength calibration, flux calibration, and the combination of the two data sets, to increase the signal-to-noise ratio (S/N). Fringing of the CCD was found to be important, and the standard defringing technique available in STSDAS was used. Defringing raised the S/N by around 15% in the red end of the spectra.

Additional steps to remove surviving cosmic rays and bad (i.e., both cold and hot pixels) pixels were performed. These additional steps are inspired by the *lineclean* task in IRAF in order to remove cold pixels and make use of a consistency check to remove cosmic rays and hot pixels (Hoyos 2002). They are explained in more detail below.

Cold pixels are flagged by fitting a sixth-degree polynomial to every line in the spectral direction of the two-dimensional spectrum. For this fit, both the 20 pixels whose DN are greatest and the 20 whose DN are lowest are discarded. The pixels whose signals are lower than the fitted polynomial value at that column by more than 3 times the rms of the fit are flagged as cold pixels. Such pixels are set to the value of the fit, and the resulting cleaned image is referred to as the partially corrected spectrum.

Hot pixels and surviving cosmic rays not removed by the standard procedures within STSDAS are identified by comparing the different spectra from the two observation data sets. First, a minimum image is created from the two data sets obtained for each source. This image does not contain any hot pixels or cosmic-ray hits, although much of the S/N is wasted.

[6] Space Telescope Science Data Analysis System (STSDAS) is a product of the Space Telescope Science Institute, operated by AURA for NASA.
[7] IRAF is distributed by the National Optical Astronomy Observatory, which is operated by AURA, Inc., under cooperative agreement with the National Science Foundation.

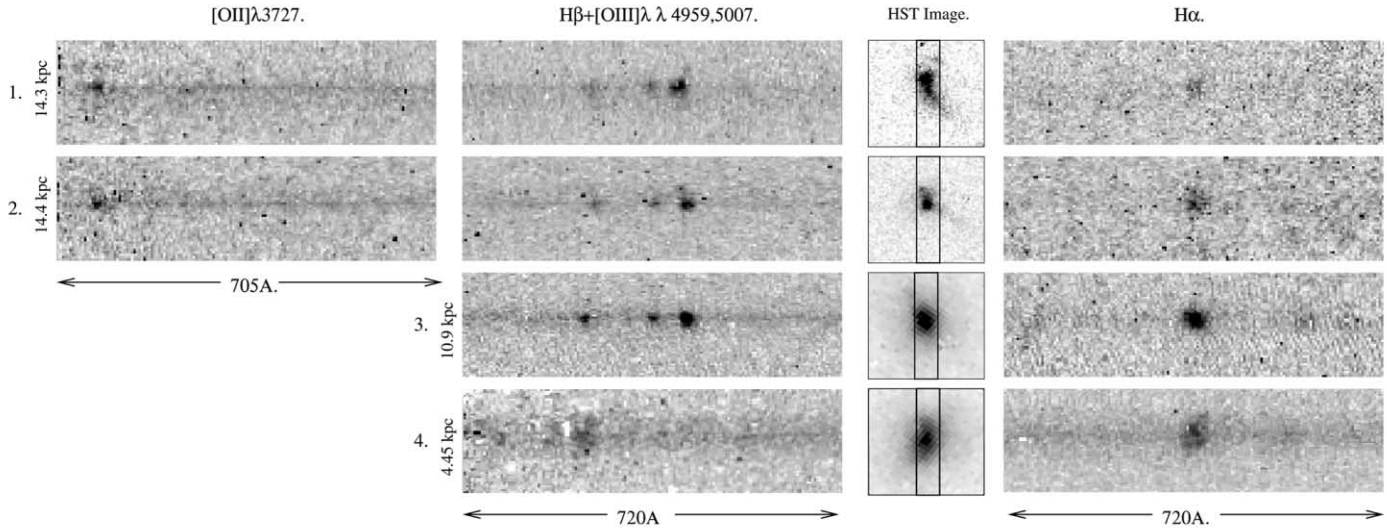

FIG. 1.—Comparison between the STIS two-dimensional spectra with *HST*/WF1 and *HST*/WFPC2 images (Koo et al. 1994; Guzmán et al. 1998). Each spectral strip spans 2″.5 in the spatial direction. The dispersion is 4.92 Å pixel^{-1}, and the spatial scale is 0″.05 pixel^{-1}. The slit orientation is shown superposed on *HST* images that are 2″.5 × 2″.5 in size.

Cold pixels from this minimum image are removed using the method outlined above. This new frame is called the minimum-corrected image. The difference between the partially corrected spectrum obtained when removing cold pixels and the minimum-corrected spectrum is therefore a spike map. Every pixel in this image brighter than 3.5 times the rms of the minimum-corrected frame calculated in a featureless area is flagged. Hot pixels and cosmic rays are removed by substituting them by their value in the minimum-corrected frame. This method has one pitfall. If a hot pixel is consistent and has the same value in both images, it will not be properly flagged.

2.1. *Description of the Spectra*

The slit placement can be seen in Figure 1. The frames for objects 1 and 2 are I814W *HST*/WFPC2 images (Guzmán et al. 1998). Images for objects 3 and 4 are F555W *HST*/WF1 data (Koo et al. 1994). In Figure 1 the spectra have been scaled and approximately aligned with the images.

Overall, the spectra are rather flat. The continuum decreases only by a factor of 2 from [O II] λ3727 to Hα. No stellar features in absorption can be observed in any case, since the continuum level is very low. The main features in the spectra are emission lines. Integrated spectra for all the sample galaxies can be seen in Figure 2.

2.2. *Errors and Uncertainties*

The three major sources of uncertainties in the emission-line measurements are (1) the readout noise of the CCD, (2) the variation of charge transfer efficiency, and (3) cosmic rays and bad pixels.

The readout noise for the STIS CCD chip for gain = 1 is 5.3 DN (rms) pixel^{-1}. This contribution is nonnegligible, since the objects under study are very faint. Typically $\sim$100 DN are accumulated per pixel in the brightest lines, and some of the measured lines reach only around 20 DN pixel^{-1} at their peaks. The continuum level is $\sim$8 DN. This effect can modify the brighter emission lines by around 5% per pixel, and the faintest lines' signal can be changed by 25% per pixel.

The STIS CCD imperfect charge transfer efficiency causes some signal to be lost when the charge is transferred through the chip at readout time. The amplifier is situated at the top right corner of the STIS CCD, making objects at lower rows appear fainter than they would if they were at high line numbers (parallel losses) and making objects on the left side of the chip appear fainter than on the right side (serial losses). This imperfection on the STIS CCD has a very negative impact for faint sources in faint backgrounds like the spectra presented here, in which less than 150 electrons are accumulated per pixel in even the brightest lines. At these levels, around 15% of the charge is lost during readout time. This imperfect parallel charge transfer efficiency then causes the observed fluxes to be seen as lower limits to the actual ones, and the serial losses also cause an artificial increase of the derived extinction coefficient from the Balmer decrement from Hα to Hβ. This latter effect is thought to be small. Because of this problem with the STIS CCD chip, the measured fluxes are to be considered as lower limits, as they may be up to 15% higher. Serial losses are believed to be less important than parallel losses.

The rate of cosmic-ray hits for the *HST* is very high. There are also a large number of bad pixels. Since the exposure times were very long because of the faintness of the observed galaxies, it is not uncommon for pixels to be hit in two different images within the same data set, making them very difficult to recover.

3. RESULTS AND ANALYSIS

3.1. *Emission-Line and Continuum Distribution*

In star-forming regions, gas and stars often follow different spatial distributions. It is then interesting to take advantage of the STIS spatial resolution to see if the continuum and the emission lines share a common spatial distribution or not. This can help to model what fraction of the mass of the system is involved in the star-forming event.

Using the IRAF task *fit1d*, a "continuum image" was made by fitting three cubic spline pieces to every line in the spectra, and then a "line image" was constructed by subtracting the continuum image from the original two-dimensional spectroscopic frame.

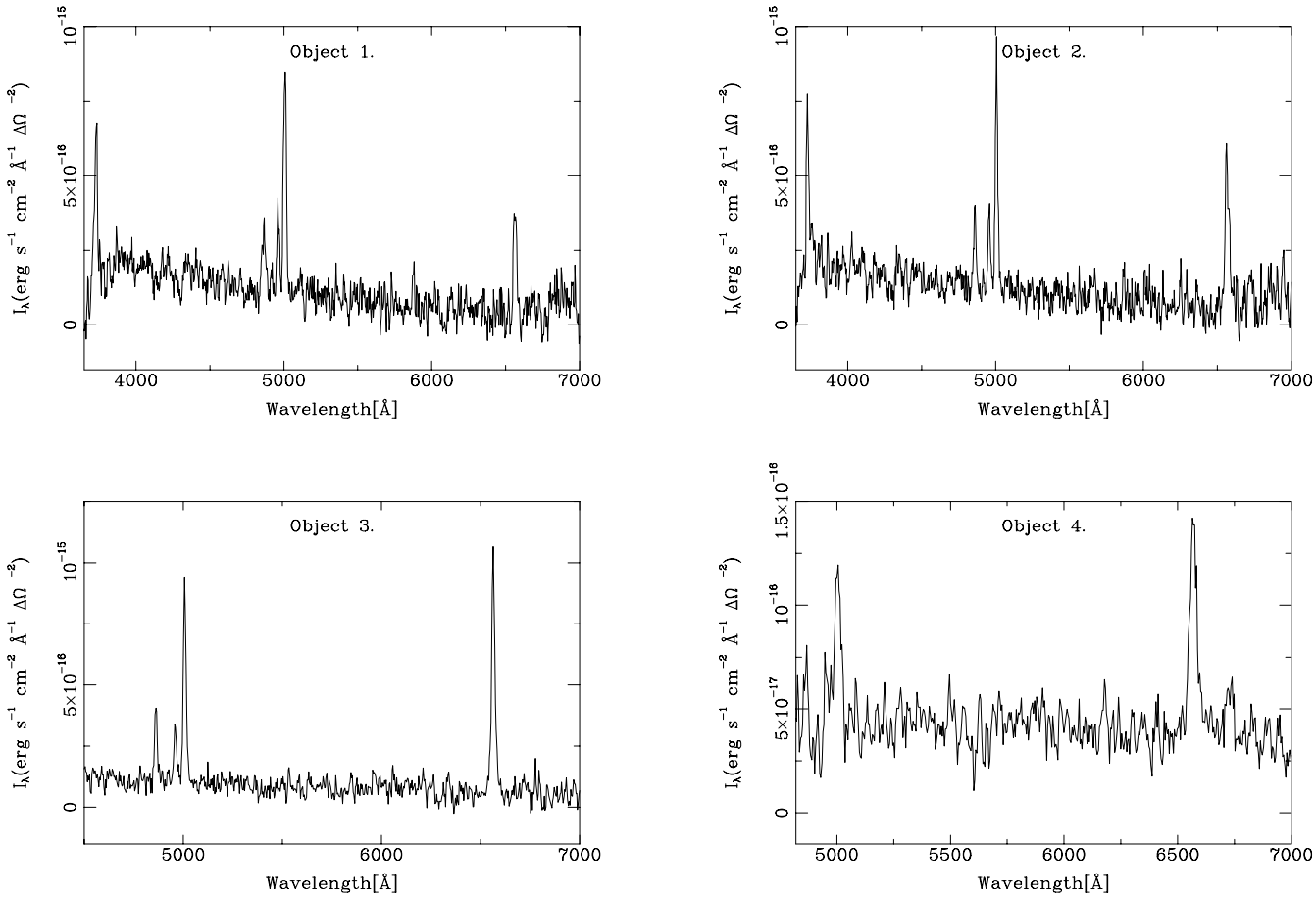

FIG. 2.—One-dimensional spectra of the four galaxies in the sample, showing the observed emission lines. Vertical axis units are ergs s^{-1} cm^{-2} arcsec^{-2} Å^{-1}.

In the spectra presented here, wavelength varies along lines, while the spatial coordinate varies along columns. The spatial distributions of both continuum and lines were investigated using the STSDAS task *ngaussfit*. This task can fit to a set of *x*-*y* values the sum of a straight line, known as the baseline, and one or several Gaussian profiles. This task also gives approximate errors for the fitted parameters, calculated by resampling.

To study the continuum spatial distribution, we fit several Gaussians to the wavelength-averaged continuum images to allow for subcomponents in the stellar population. In all cases the sum of two Gaussians provided a good fit to the continuum data. For the emission lines, we tried a two-Gaussian fit similar to that performed for the continuum. However, only object 2 had enough substructure with high S/N in the line-emitting region for the best fit to require the sum of two Gaussians. Objects 1, 3, and 4 did not have enough S/N or evidence for substructure to distinguish several components, and thus only one Gaussian is fitted. In summary, the procedure to choose how many Gaussians should be used to fit any given profile is as follows. First of all, a single Gaussian is fitted, and the residuals are plotted. If these residuals, when compared to the statistical error of the data, still show evidence for a nonzero substructure, a new model with two Gaussians is tried. This process could be iterated, but it was found that two Gaussians were always enough. The continuum profile is the result of averaging around 1000 columns, and the line-emitting profile is obtained by collapsing only a few; therefore the statistical error in the former case is proportional to $1/(1000)^{1/2}$, and this error in the latter case is proportional to $1/(\text{a few})^{1/2}$. This recipe naturally leads to the continuum being fitted by two Gaussians and to the line-emitting region being fit by a single Gaussian model in most cases. The exception is the emission region of object 2, in which the second iteration is clearly needed, as can be seen in Figure 3.

Table 2 lists the central position of the line-emitting region with respect to the continuum center and the spread (i.e., width) of both the continuum-emitting region and the line-emitting region.

For single-Gaussian fits, the centroid is just the Gaussian central position, but for double-Gaussian fits, the centroid $\bar{x}$ is calculated as

$$\bar{x} = \frac{A_1 x_1 + A_2 x_2}{A_1 + A_2}, \tag{1}$$

where x_i is the central position of the ith Gaussian and A_i is its amplitude.

The line central positions given in Table 2 are calculated with respect to the continuum centroid.

The spread of single Gaussian fits is defined as simply the FWHM of the Gaussian, while for double-Gaussian fits the spread is defined as

$$\text{spread} = |x_2 - x_1| + \frac{A_1 \text{FWHM}_1 + A_2 \text{FWHM}_2}{A_1 + A_2}, \tag{2}$$

where x_i is the central position of the ith Gaussian, A_i is its amplitude, and FWHM_i is its full width at half-maximum.

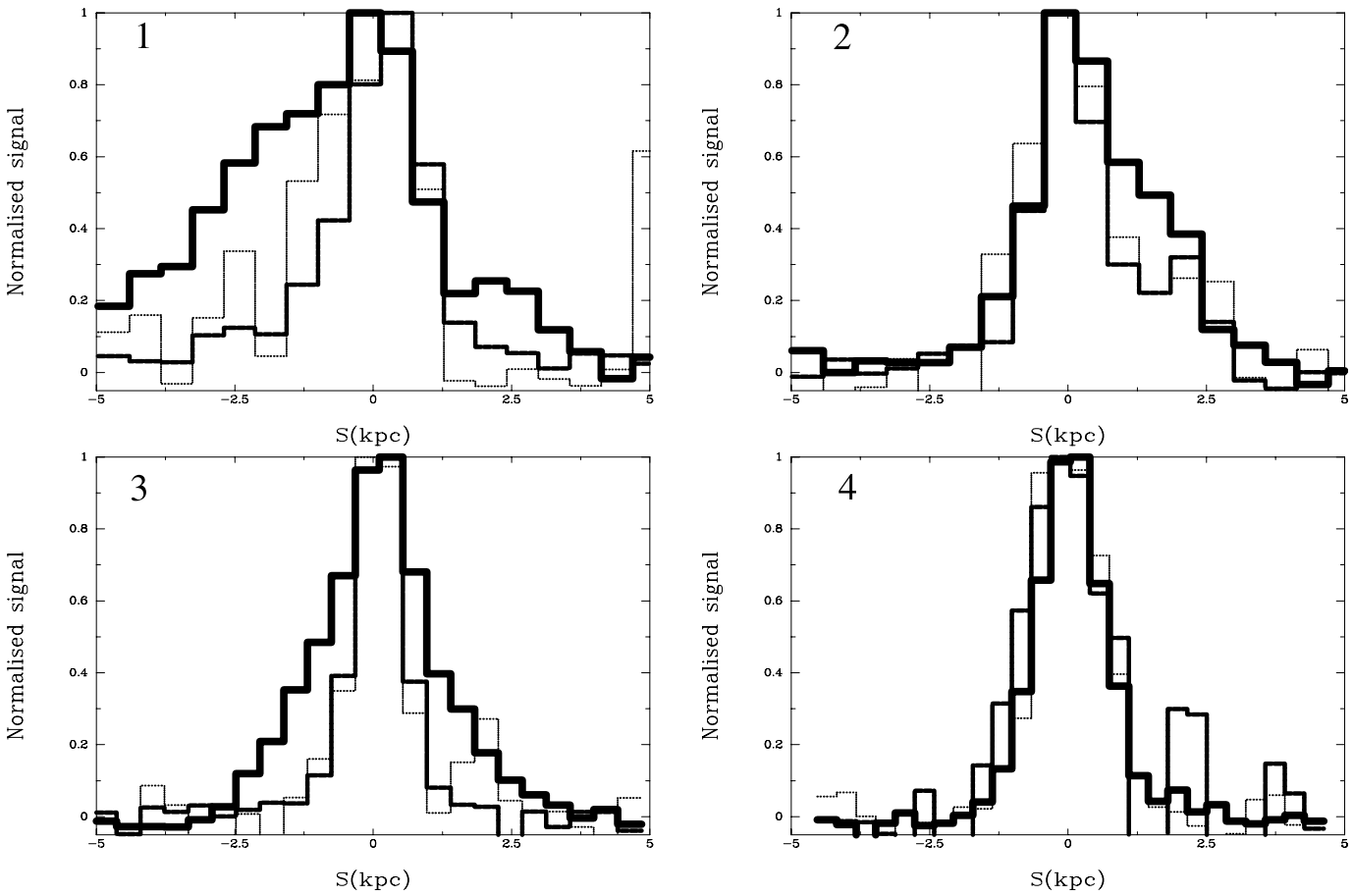

FIG. 3.—Continuum and emission-line spatial profiles. In all cases, the *S*-axis is placed with respect to the slits depicted in Fig. 1. Increasing *S* corresponds to upper positions in that figure for each object. The continuum is the thickest solid line; [O III] λ5007 is the thick line; and Hβ is the dotted line.

(This number equals the FWHM in the case of single-Gaussian fits.) All values in this table are given in arcseconds. From its definition, in the case of two equal-intensity Gaussians of equal width, the spread is the FWHM plus the difference in the centroid values of the two Gaussians.

The spatial profiles in Figure 3 show the fitted data in histogram form. When plotting the continuum distributions, the baseline component is subtracted in order to show only the Gaussian parts of the fits.

From Figure 3 and Table 2, it can be seen that

1. Object 1 shows two interesting features. (1) The nebular component center does not coincide with the continuum centroid. The offset is about one-third the size of the emission lines themselves. (2) The spread of the continuum is about 3 times that of the emission-line component. This is interesting because optically (Guzmán et al. 1998) this galaxy presents both a knot (coincident with the observed line-emitting region in the

TABLE 2
SPATIAL DISTRIBUTION DATA

ID	Scale (kpc arcsec^{-1})	Continuum Spread (arcsec)	Line	Line Central Position[a] (arcsec)	Line Spread (arcsec)	spread$_{line}$/spread$_{cont}$[b]
1.....	5.68	0.84 ± 0.02	[O II] λ3727	0.15 ± 0.01	0.20 ± 0.02	0.24
		0.84 ± 0.02	Hβ	0.10 ± 0.03	0.37 ± 0.02	0.44
		0.84 ± 0.02	[O III] λ5007	0.154 ± 0.005	0.298 ± 0.009	0.35
		0.84 ± 0.02	Hα	0.14 ± 0.02	0.46 ± 0.04	0.55
2.....	5.70	0.56 ± 0.02	[O II] λ3727	−0.03 ± 0.01	0.30 ± 0.02	0.52
		0.56 ± 0.02	Hβ	−0.03 ± 0.02	0.68 ± 0.09	1.20
		0.56 ± 0.02	[O III] λ5007	−0.016 ± 0.005	0.582 ± 0.009	1.03
		0.56 ± 0.02	Hα	−0.05 ± 0.05	0.6 ± 0.1	1.06
3.....	4.31	0.59 ± 0.01	Hβ	0.00 ± 0.01	0.211 ± 0.008	0.36
		0.59 ± 0.01	[O III] λ5007	0.008 ± 0.003	0.241 ± 0.004	0.41
		0.59 ± 0.01	Hα	−0.003 ± 0.005	0.296 ± 0.006	0.50
4.....	1.76	0.79 ± 0.01	[O III] λ5007	−0.10 ± 0.03	0.90 ± 0.03	1.14
		0.79 ± 0.01	Hα	0.00 ± 0.01	0.82 ± 0.02	1.04

[a] Difference between line and continuum centroids. Positive values indicate that the line-emitting component is above the continuum in the spectra shown in Fig. 1.
[b] Line/continuum spread ratio.

spectrum) and a tail. This seems to indicate that the starburst does not involve all the optical host galaxy but is concentrated on one end of it. It also indicates the presence of a very important underlying population. Figure 3 also shows that Hβ and [O III] λ5007 occupy a common region within the source. This object is very similar to the so-called "cometary blue compact dwarfs" in the nearby universe (Noeske et al. 2000).

2. For object 2, the differences in the centroid positions for the continuum and the emission components are much smaller than the spread of both. The centroid positions are also very similar. Figure 3 in fact shows that the line-emitting component and the continuum-emitting component trace each other rather well. Figure 3 also suggests that this galaxy consists of two different subsystems separated by around 1.3 kpc. The star-forming region would be weaker relative to the underlying continuum in the fainter subsystem than in the more luminous one. The *HST*/WFPC2 observations from Guzmán et al. (1998) reveal that optically this galaxy appears to have two knots of star formation. This is consistent with Figure 3.

3. In object 3, the continuum and the line-emitting component can be said to share a common center, well within their respective distributions. The spatial extent of the oxygen and hydrogen emission are found to be about the same, while the continuum size is clearly larger than that of the line-emitting region, as is seen in Figure 3. Optically (Koo et al. 1994) this galaxy appears as a single knot, which suggests that the star-forming region is confined to the central part of the galaxy.

4. For object 4, the distributions of the continuum, [O III] λ5007, and Hα emission are clearly coincident. In *HST*/WF1 observations from Koo et al. (1994), a single knot is identified. These two facts suggest that the starburst is in this case widespread.

Of the three error sources discussed in § 2.2 above, none of them can affect the results presented in this section to a large extent. Bad pixels and surviving cosmic rays are rejected from the fit by a rejection algorithm. The readout noise is taken into account by the constant coefficient of the baseline and its importance further reduced during the fitting procedure, as several columns are to be collapsed. (To fit the continuum image, around 1000 columns are co-added, while to fit the emission component, about six lines are collapsed.) Finally, the parallel charge transfer inefficiency does not affect the conclusions of this section, since the Gaussian fits are normalized, and serial charge loss does not affect the measurements performed on the line image, since this error source is unimportant on scales of a few columns.

In all cases but the last, the spreads of [O III] λ5007 and Hβ are compared, discarding Hα and [O II] λ3727. This is done because [O III] λ5007 and Hβ are closer to each other in wavelength space and therefore they are affected by a similar extinction. Differences in their spreads can then reveal real differences in their distributions and not just reddening. The observed differences in the spread of Hα and Hβ or [O III] λ5007 and [O II] λ3727 can be accounted for by a moderate extinction, within the measurement errors. The spread values given in Table 2 do not take into account the error introduced by the extinction error. This uncertainty makes it impossible to detect unambiguously any extinction gradient or ionization structure. No differences in the spatial extent of H II and O II or O III can be established either. In all four cases, then, the line-emitting component does not reveal any composition differences. Table 2 lists in its last column the ratio of the spread of the corresponding emission line to that of the continuum. The large scatter of values in the relative sizes of nebular emission and the continuum indicates that LCBGs are a very inhomogeneous population.

It should be noted that the continuum image is constructed based on the *observed* spectrum (i.e., not dereddened). The real continuum has more power in shorter wavelengths, and the actual shape of the normalized continuum will be slightly different. Therefore, although the actual numbers may change, the main results are robust. This is true even if the serial charge loss were important, since it would mimic an increase in the extinction coefficient.

It is also interesting to note that not all starbursts are located in the center of their host galaxies as parametrized by the continuum light distribution (e.g., object 1). Some questions naturally arise; for instance, what mechanisms could trigger such a massive star-forming event displaced from the center of the host galaxy? How does this diversity affect the evolutionary scenarios of these objects? More data are needed to characterize the frequency of these off-center star-forming regions and their effect on the morphological evolution of LCBGs.

3.2. *Line Ratios, Reddening, and Equivalent Widths*

The observed flux in each emission line has been measured by means of a Gaussian fit, using again the STSDAS task *ngaussfit*. This fitting procedure was used instead of summing the flux in the line image directly because of residuals of bad pixels. Observed line surface brightnesses are calculated using the amplitude and full width at half-maximum yielded by *ngaussfit* simply as 1.064(amplitude)(FWHM), which is the expression for the area under a Gaussian given its amplitude and full width at half-maximum. Two different positions are considered for each galaxy corresponding to (1) the inner and (2) the outer regions of each object. These two one-dimensional extractions are defined to encompass approximately the same line luminosity. For position (1), both the central wavelength and FWHM are left as free parameters, but for position (2) the FWHM is fixed to that measured in position (1) in order to increase the goodness of the fit. The physical sizes of the two extractions considered are given in Table 3. The sum of the two quantities is therefore the total physical size of the observed line-emitting region.

The [O II] λ3727 line can be observed in objects 1 and 2, Hβ and [O III] $\lambda\lambda$ 4959, 5007 can be observed in all cases (although see comments to Table 3), and Hα is observed in objects 2, 3, and 4. Hα is detected in object 1 as well, but it is affected by several bad pixels that make it unrecoverable. It can be seen in Figure 2 that the amplitude of Hα is only about twice that of Hβ, although it should be at least 3 times larger. The [S II] $\lambda\lambda$6717, 6731 lines are observed only in the nearest object.

The amount of extinction can be parametrized using the logarithmic extinction coefficient c(Hβ). It is derived through standard nebular analysis techniques (Osterbrock 1989) using Balmer line ratios. The observed targets are at high Galactic latitude, suffering Galactic extinctions $A_B < 0.11$ mag, which corresponds to a $c(\mathrm{H}\beta) < 0.05$ (Burstein & Heiles 1984; Sandage & Tamman 1974). Therefore, it is assumed that all the extinction occurs within the target objects. Consequently, the spectra have been dereddened in the rest frame of the target, according to a standard reddening curve (Whitford 1958), assuming case B recombination theoretical line ratios. The use of different extinction curves would not significantly change the results, since they do not differ from the one used here in the wavelengths of interest.

The logarithmic extinction coefficient is determined independently for the inner and outer regions for objects 2 and 3, but

TABLE 3

Absorption Coefficients, $W_{H\beta}$, and Dereddened Line Strengths/Ratios

ID	1	1	2	2	3	3	4	4
Position	Inner	Outer	Inner	Outer	Inner	Outer	Inner	Outer
Size[a]	1.42	3.41	1.43	2.28	0.86	2.16	0.79	1.23
$c(H\beta)$	0.10 ± 0.05	0.10 ± 0.05	0 ± 0.1	0.10 ± 0.2	0.4 ± 0.1	0.7 ± 0.2	0.6 ± 0.2	0.6 ± 0.2
$\log W^0_{H\beta}$[b]	1.68 ± 0.09	1.57 ± 0.07	1.59 ± 0.03	1.51 ± 0.05	1.71 ± 0.04	1.48 ± 0.07	1.55 ± 0.09	1.55 ± 0.09
[O II] λ3727[c]	5 ± 1	4.3 ± 0.8	2 ± 1	2 ± 1	...	...	...	...
Hβ[c]	2.1 ± 0.5	2.3 ± 0.4	1.4 ± 0.5	1.6 ± 0.7	5 ± 1	6 ± 3	5 ± 3	5 ± 3
[O III] λ4959[c]	2.6 ± 0.6	2.0 ± 0.5	1.7 ± 0.6	1.0 ± 0.5	4 ± 1	5 ± 3	5 ± 3	5 ± 3
[O III] λ5007[c]	8 ± 2	6 ± 1	5 ± 1	3 ± 1	13 ± 3	16 ± 7	15 ± 9	15 ± 9
Hα[c]	...	...	4 ± 1	4 ± 1	13 ± 2	17 ± 5	15 ± 6	14 ± 5
[S II] $\lambda\lambda$6717, 6731[c]	...	...	...	...	...	...	3 ± 1	2 ± 1
log(([O III] $\lambda\lambda$4959, 5007)/Hβ)	0.7 ± 0.1	0.54 ± 0.08	0.67 ± 0.03	0.44 ± 0.06	0.56 ± 0.03	0.55 ± 0.07	0.6 ± 0.1	0.61 ± 0.09
log([O III]/[O II])	0.28 ± 0.09	0.26 ± 0.07	0.43 ± 0.06	0.33 ± 0.09	0.3 ± 0.1	0.1 ± 0.1	0.2 ± 0.1	0.2 ± 0.1
log R_{23}[d]	0.89 ± 0.08	0.73 ± 0.06	0.80 ± 0.03	0.61 ± 0.05	0.72 ± 0.04	0.79 ± 0.07	0.8 ± 0.1	0.8 ± 0.1

Notes.—For object 1, Hα is not observed, and the listed value for the logarithmic extinction coefficient is an *assumed* value, typical for local H II galaxies. For object 4, Hβ and [O III] λ4959 are only measured for the integrated spectra because of several bad pixels that make them unfeasible to measure on a per position basis; for this object, the given values for $c(H\beta)$ and $\log W^0(H\beta)$ correspond to the integrated spectra, and the listed dereddened fluxes for the aforementioned lines are just one half of the integrated spectra values.

[a] In kiloparsecs.

[b] In angstroms.

[c] In units of 10^{-16} ergs s^{-1} cm^{-2}. Fluxes are apparent fluxes.

[d] The value R_{23} is defined as the reddening-corrected ratio ([O II] λ3727 + [O III] $\lambda\lambda$4959, 5007)/Hβ.

for object 4, because of poor S/N, a global value is adopted. In the case of object 1, for which Hα is unfortunately not well measured, a global value of $c(H\beta) = 0.1 \pm 0.05$, typical for local H II galaxies, is adopted. No underlying stellar hydrogen absorption is detected, as the continuum is very low. The observed extinction coefficients are given in Table 3. Assuming $A_B = 4.3E(B-V)$ (see Burstein & Heiles 1984), the $B-V$ color excess ranges from 0 to 0.35.

Line fluxes are then dereddened using the standard expression

$$I(\lambda)_{\rm corrected} = I(\lambda)_{\rm obs} 10^{c(H\beta)[1+f(\lambda)]}. \quad (3)$$

Table 3 lists the dereddened line strengths, along with the measured Hβ equivalent width and the derived extinction coefficient $c(H\beta)$.

Line ratios are then calculated according to

$$\left(\frac{I_1}{I_2}\right)_{\rm corr} = \frac{I_{1,\,\rm obs}\left[1 + (\Delta I_{2,\,\rm obs}/I_{2,\,\rm obs})^2\right]}{I_{2,\,\rm obs}} \times 10^{c(H\beta)[f(\lambda_1)-f(\lambda_2)]}. \quad (4)$$

The rationale behind the factor $1 + (\Delta I_{2,\,\rm obs}/I_{2,\,\rm obs})^2$ is explained in the Appendix, whereas the factor $10^{c(H\beta)[f(\lambda_1)-f(\lambda_2)]}$ is used to deredden the line ratio. For SA68-6134 and H1-13385, [O II] λ3727 is not observed. Based on the fact that a relation seems to exist between ionization parameter and equivalent width of Hβ for local H II galaxies (Díaz 1998), we used the following, which represents a linear fit for a sample of H II galaxies, to estimate [O II] λ3727:

$$\log \frac{[\rm O\,III]}{[\rm O\,II]} = (0.877 \pm 0.042) \log W_{H\beta} - 1.155 \pm 0.078. \quad (5)$$

The rms in the fit is indicated by the given errors. Table 3 lists the dereddened line ratios. It can be seen that line ratios are less affected by uncertainties in the determination of $c(H\beta)$ than line strengths are.

In principle, oxygen abundances can be estimated from the intensities of the optical emission lines using the R_{23} number, defined as the reddening-corrected ratio ([O II] λ3727 + [O III] $\lambda\lambda$4959, 5007)/Hβ (Pagel et al. 1979). The main problem with this empirical method is that the calibration is double-valued and some a priori knowledge of the metallicity range is needed in order to solve this degeneracy. Unfortunately, because of the poor S/N, no reliable metallicity determinations can be derived for the LCBGs presented here. However, the ionization ratio $\log([\rm O\,III]/[\rm O\,II])$ and R_{23} values given in Table 3 allow us to draw some very general conclusions. First of all, extremely low $[12 + \log(\rm O/H) < 7.6]$ or supersolar $[12 + \log(\rm O/H) \geq 8.7]$ abundances can be ruled out. Also, since it would be very unlikely that the inner and outer parts of the line-emitting region fell in different branches of the $R_{23} - 12 + \log(\rm O/H)$ calibration, strong spatial variations of the metal content can be ruled out.

Equivalent widths are calculated from *ngaussfit* results as

$$W = \frac{I\left[1 + (\Delta C/C)^2\right]}{(1+z)C}, \quad (6)$$

where C is the baseline value at the central wavelength of the corresponding emission line and the factor $1+z$ transforms the equivalent width to the rest frame. The $1 + (\Delta C/C)^2$ is used for the same reason as in the case of the line ratios and is again explained in the Appendix. The measured rest-frame Hβ equivalent widths are between 30 and 50 Å, within the observed range for H II galaxies, indicating either that the observed burst cannot be very young or that a substantial underlying stellar population must be present.

The most important source of errors in the derived line strengths for these data is the uncertainty in the determination of $c(H\beta)$. The main systematic error that may affect the extinction coefficient is the serial charge transfer inefficiency, which may increase its value. However, the measurement of

TABLE 4
STAR FORMATION PARAMETERS AND VIRIAL MASS ESTIMATES

ID	Position	SFR ($M_\odot$ yr^{-1})	SFR$_A$ ($M_\odot$ yr^{-1} kpc^{-2})	$D_{\rm eff}$ (kpc)	D_0 (kpc)[a]	log $M/M_\odot$
1.....	Inner	3.2 ± 0.7	2.1 ± 0.3	5.4	1.42	9.8
	Outer	3.6 ± 0.7	...	...	...	...
2.....	Inner	2.2 ± 0.7	1.5 ± 0.4	4.2	1.43	9.7
	Outer	2.5 ± 1.0	...	...	...	...
3.....	Inner	2.6 ± 0.6	5.0 ± 2.0	2.0	0.86	9.3
	Outer	3.3 ± 1.7	...	...	...	...
4.....	Inner	0.25 ± 0.10	0.5 ± 0.1	1.4	0.79	9.6
	Outer	0.24 ± 0.09	...	...	...	...

NOTES.—Since the areal star formation, half-light radii, and mass are properties of the galaxy as a whole, they are listed only once for each galaxy. The results presented here are mainly affected by the parallel losses of the STIS/CCD and may be underestimating the real values by around 15%. Statistical errors are again dominated by the CCD's readout noise.

[a] The effective diameter of the line-emitting region given here is the size of the (1) aperture defined previously. It is equivalent to the half-light radius of a bidimensional Gaussian luminosity distribution of the same full width at half-maximum.

a zero extinction coefficient in zone (1) of object 2, together with the comparison of the $c(\mathrm{H}\beta)$ value with that reported by Kobulnicky & Zaritsky (1999) for the same object using LRIS on the W. M. Keck Telescope, suggests that this serial loss is not very important and would, in any case, introduce an increase in the extinction coefficient of less than 0.1. Line ratios and equivalent widths are much less affected than line strengths by this uncertainty.

On the other hand, parallel losses may introduce a systematic decrease of around 15% in the observed line strengths, as previously noted. The values quoted in Table 3 are not corrected for this systematic error and should therefore be regarded as lower limits to the true values.

The statistical error budget is again dominated by the readout noise, which is the most important per pixel statistical uncertainty source for the data. The Poisson photon noise is only important for the brightest lines such as [O III] λ5007 and Hα. Outliers such as bad pixels and cosmic rays are excluded from the fit by the *ngaussfit* rejection algorithm. The error estimates provided by this task are considered as 1 σ error bars.

3.3. *Star Formation Rate and Structural Parameters of Star-Forming Regions*

The main aim of this study is to investigate the nature of LCBGs. In this section, the intermediate-z sample analyzed here is compared with two samples of local, vigorously star-forming systems.

The first sample is made of 39 local H II galaxies from the Telles et al. (1997) sample. These galaxies are among the brightest ones in the Spectrophotometric Catalogue of H II Galaxies (SCHG; Terlevich et al. 1991), with equivalent widths between 30 and 280 Å. This sample is made of H II galaxies of different morphologies. The velocity dispersions range from 20 to 130 km s^{-1}, although with a preference for the lower values.

The other sample consists of 25 starburst galaxies from the Lehnert & Heckman (1996) sample. The galaxies from this latter sample are edge-on (with axial ratios a/b greater than 2),[8] infrared warm ($S_{60\ \mu\mathrm{m}}/S_{100\ \mu\mathrm{m}} > 0.4$), and infrared bright ($S_{60\ \mu\mathrm{m}} > 5.4$ Jy). The infrared luminosity of this sample ranges from 10^{10} to 10^{12} $L_\odot$. This sample consists of a mixture of spiral (Sa–Sd), lenticular, and irregular galaxies. The rotation speeds range from around 120 to approximately 300 km s^{-1}.

The first local sample was chosen for comparison purposes, since H II galaxies are known to show conspicuous and galaxy-wide emission line spectra. They are quite similar to the LCBGs presented here in this regard, as suggested by Koo et al. (1994) and Guzmán et al. (1997). Furthermore, their velocity dispersions and small radii imply that they should be about as massive as the galaxies analyzed here. They are also known to harbor violent star-forming systems as do intermediate-z LCBGs.

The second local sample was selected because these starburst galaxies also host powerful and galaxy-wide star-forming complexes, although they are much larger systems. These starburst galaxies are not only bigger, but their rotation speeds are greater than typical velocity dispersions of H II galaxies or LCBGs at intermediate z. These systems are likely to be more massive, and their global star formation rate should be accordingly higher.

Table 4 contains the star formation rate, the star formation rate per unit area, and the half-light radii of both the galaxy and the line-emitting region.

Calculated Hβ luminosities lie in the range $0.2\text{–}2.7 \times 10^{41}$ ergs s^{-1}. These luminosities are in the high-luminosity tail of the distribution for normal spiral galaxies (Kennicutt 1983) and H II galaxies (Hoyos & Díaz 2004).

The star formation rates were calculated from the Hα luminosity as in Kennicutt et al. (1994), valid for $T_e = 10^4$ K and case B recombination (all the ionizing photons are processed by the nebular gas):

$$\mathrm{SFR}(M_\odot\ \mathrm{yr}^{-1}) = 7.9 \times 10^{-42} L_{\mathrm{H}\alpha}(\mathrm{ergs\ s}^{-1}). \quad (7)$$

The calculated star formation rates are in the range from 0.5 to 7 $M_\odot$ yr^{-1}, indicating that the star-forming regions are very strong. For comparison, the 30 Doradus SFR is 0.1 $M_\odot$ yr^{-1}, as derived from its Hα luminosity (Schaerer 2002).

A most interesting quantity is the star formation rate per square kiloparsec, the areal star formation rate. This is directly proportional to the Hα surface brightness, after correcting for

[8] The expression a is the length of the major axis, and b is the length of the minor axis.

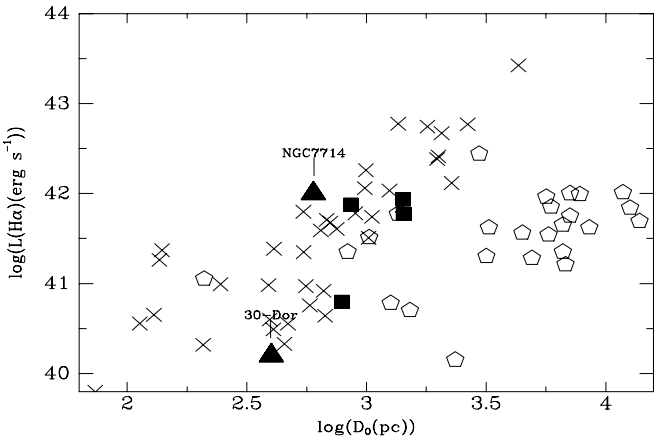

FIG. 4.—Star-forming region size–Hα luminosity relationship: *Crosses*, local H II sample; *squares*, intermediate-z LCBGs; *triangles*, 30 Dor nebula and circumnuclear H II region in NGC 7714; and *pentagons*, local starburst galaxies sample (Lehnert & Heckman 1996). The value D_0 is the *burst* half-light diameter for the Telles et al. (1997) and Lehnert & Heckman (1996) samples and the diameter of the inner aperture for the LCBG sample.

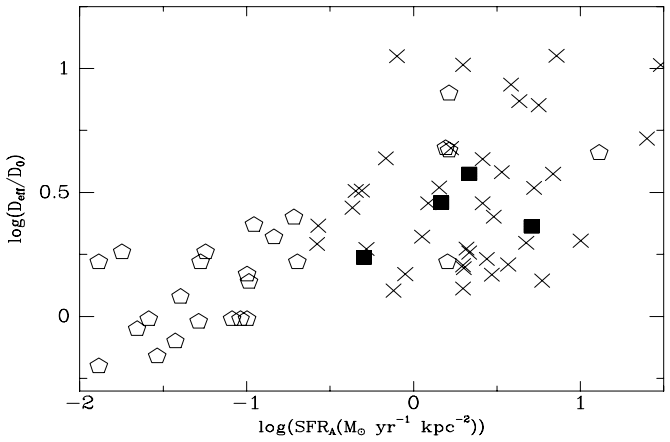

FIG. 5.—Galaxy size to burst size ratio vs. SFR_A. Symbols are as in Fig. 4.

cosmological dimming. For the intermediate-z sample and for the Lehnert & Heckman (1996) sample, the expression used is

$$\mathrm{SFR}_A\left(\frac{M_\odot\ \mathrm{yr}^{-1}}{\mathrm{kpc}^2}\right) = \frac{2\times 7.9\times 10^{-42} L_{\mathrm{H}\alpha}}{\pi D_0^2}, \qquad (8)$$

where $L_{\mathrm{H}\alpha}$ is the reddening-corrected Hα luminosity (in ergs s^{-1}) and D_0^2 is the half-light diameter of the line-emitting region (in kiloparsecs). For the LCBGs presented here, D_0 is defined as the size of the central extraction (1), defined previously. Since it contains 50% of the line luminosity from the starburst, it can be considered as the half-light radius of the line-emitting region. In the case of the starburst galaxies from the Lehnert & Heckman (1996) sample, D_0 is the line-emitting region effective diameter, as measured in narrowband Hα + [N II] images, which trace the size and luminosity of the starburst. In order to derive the Hα luminosity for this sample from the values listed in Lehnert & Heckman (1996), it is necessary to correct for internal extinction and for [N II] λ6584 contamination. A simple statistical approach was adopted such that $L_{\mathrm{H}\alpha\ \mathrm{corr}} = 1.56 L_{\mathrm{H}\alpha\ \mathrm{listed}}$.[9]

The areal star formation rate for the Telles et al. (1997) sample is calculated by

$$\mathrm{SFR}_A\left(\frac{M_\odot\ \mathrm{yr}^{-1}}{\mathrm{kpc}^2}\right) = \frac{7.271\times 10^{c(\mathrm{H}\beta)} F_{\mathrm{H}\beta}(1+z)^4}{D_0^2}, \qquad (9)$$

where D_0 is the line-emitting region effective diameter (in arcseconds), as observed in the V band. The expression $F_{\mathrm{H}\beta}$ is the *observed* Hβ flux, while the other factors account for the cosmological dimming and internal reddening. The burst half-light radii given in Telles et al. (1997) are the FWHMs of the circular brightness profiles centered on the peak intensity of the burst region of the galaxy, after correcting for seeing effects.

In order to compare the properties of the star-forming regions in LCBGs with those of the local samples of star-forming systems, two plots are presented. Figure 4 shows the Hα luminosity plotted versus the *burst* half-light diameter. Figure 5 shows the ratio of the *galaxy* half-light diameter and the *line-emitting* region half-light diameter (D_{eff}/D_0) for the galaxies from Telles et al. (1997), Lehnert & Heckman (1996), and for the intermediate-z galaxies versus the areal star formation rate SFR_A.

From Figures 4 and 5 it is seen that the intermediate-z galaxies presented here are very similar to the galaxies from the sample of bright local H II galaxies. The star-forming region size scales with the host galaxy size in a similar fashion in LCBGs and in their local counterparts of similar areal star formation rate. This indicates similar morphological properties between H II galaxies and LCBGs. The Hα luminosity of intermediate-z LCBGs is similar to the Hα luminosity of bright local H II galaxies with similar line-emitting region sizes. The starburst galaxies from the Lehnert & Heckman (1996) sample have a much lower areal star formation rate. Despite having star-forming regions around 6 times larger on average, their star formation rates do not exceed the observed rates in the intermediate-z objects or bright local H II galaxies. This happens even though the fraction of the host galaxy occupied by the burst is 3 times larger in starburst galaxies than in LCBGs or H II galaxies.

Figure 4 also shows two well-known examples of violent star formation in the nearby universe. NGC 7714 (González-Delgado et al. 1995) is a starburst galaxy classified as SBb peculiar by de Vaucouleurs et al. (1991). It is interacting with NGC 7715. Most of the galaxy is undergoing a major starburst, which is unusually active in the nucleus, where the star formation rate per unit area is very high. The object 30 Dor is a large star-forming region in the Large Magellanic Cloud. It is the nearest object in which violent star formation can be studied in detail. Figure 4 shows the star-forming regions of LCBGs are all larger than both the circumnuclear star-forming regions in NGC 7714 and 30 Dor. The Hα luminosity of the line-emitting region of LCBGs varies from 3 to 50 times that of 30 Dor. Three out of four have Hα luminosities similar to the central region of NGC 7714. We conclude that the star-forming regions found in LCBGs, although extreme, are not rare in the local universe, since they are found not only in the brightest H II galaxies but in other vigorously star-forming systems as well.

Another very useful parameter in studying the nature of distant, young galaxies is mass, since mass is much less dependent on evolution than luminosity or colors. Galaxies of the same mass can be compared independently of the evolutionary stage of their stellar populations. Mass estimates are

[9] This is just the average value of the number $10^{0.63c(\mathrm{H}\beta)}/(1+[\mathrm{N\,II}]\ \lambda 6584/\mathrm{H}\alpha)$ when the extinction varies from 0.2 to 0.6 and the nitrogen-to-hydrogen ratio varies from 0.01 to 0.32.

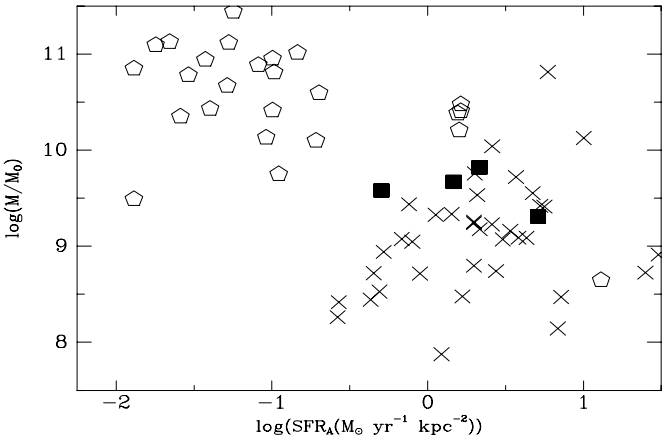

FIG. 6.—Mass–areal star formation rate relationship. Symbols are as in Fig. 4.

obtained via the virial theorem, using the half-light radius and velocity width as measures of galaxy size and gravitational potential:[10]

$$\log M/M_\odot = 6.08 + \log R_e(\mathrm{kpc}) + 2\log\sigma(\mathrm{km\ s^{-1}}). \quad (10)$$

For the LCBGs analyzed here, the half-light radii are given in Koo et al. (1994) and Guzmán et al. (1998). The velocity dispersions are taken from Guzmán et al. (1996) and Koo et al. (1995). For the H II galaxies sample, both the effective radius and the velocity dispersion are given in Telles et al. (1997). For starburst galaxies from the Lehnert & Heckman (1996) sample, the velocity dispersion is set to 0.7 times the rotation speed, following Phillips et al. (1997), and inclination effects are partially corrected for by multiplying the rotation speed by $[1-(a/b)^{-2}]^{1/2}$. This correction assumes all these galaxies are circular in shape.

Figure 6 shows the virial mass estimates plotted against the areal star formation rate. In this diagram LCBGs also fall among the brightest, more massive H II galaxies. It is also seen that intermediate-z LCBGs present a much higher areal star formation rate than local starburst galaxies of similar mass. On the other hand, LCBGs tend to have masses consistent with the low-mass end distribution of the Lehnert & Heckman (1996) sample. Even if local starburst galaxies have larger star-forming regions (as is shown in Fig. 4) and are much more massive, their areal star formation rate does not rival that of LCBGs and bright H II galaxies. We conclude that the properties of star-forming regions in LCBGs at intermediate redshift are very similar to those found in the local universe in very bright and massive H II galaxies like Tol 0440-381 or starburst galaxies like NGC 1808 with similar star formation properties.

4. SUMMARY

We have used spatially resolved STIS long-slit spectroscopy to investigate the nature of four LCBGs at intermediate z. In particular we have shown that the distributions of the continuum and emission lines along the spatial direction indicate that the starburst usually occupies more than 50% of the continuum-emitting region. LCBGs have properties very similar to the star-forming regions of high-luminosity H II galaxies. It has also been found that the LCBGs at intermediate z presented do not show unusually high star formation rates per unit area, although they are more massive than the average H II galaxy of similar star formation rate per unit area.

C. H. wishes to thank UCO/Lick for hospitality, friendship, and a wonderful 2002 summer/fall. He is also grateful to the University of Florida and the folks over there for an unforgettable 2001 fall. He is also grateful to Marcelo Castellanos. This work has been partially supported by the Spanish DGCyT grant AYA-2000-0973 and the Spanish MECD FPU grant AP2000-1389. R. G. acknowledges funding from NASA/STScI grant HST-GO-08678.04-A and LTSA NAG5-11635. M. A. B. also acknowledges support from NASA/STScI grant HST-GO-08678.04-A, as well as NASA/STScI grant GO-9126 and NASA/LTSA NAG5-6032. We are grateful to Kai G. Noeske for comments and advice. We are also very grateful to the anonymous referee whose comments helped to improve the final version of this paper.

APPENDIX

QUOTIENTS BETWEEN LOW-S/N RANDOM VARIABLES

It is possible to derive an approximate expression that is useful for calculating ratios between two quantities when the S/N of the denominator is very low.

Let a and b be two random variables, and let c be their quotient. The mean value of c is

$$\bar{c} = \int \frac{a}{b} f(a,b)\, da\, db, \quad (A1)$$

where $f(a, b)$ is the joint probability density.

If the random variables a and b are independent, this can be expressed as

$$\bar{c} = \bar{a} \int \frac{1}{b} f_b(b)\, db, \quad (A2)$$

where $f_b(b)$ is the probability density of b.

If a Taylor polynomial is fit to $1/b$ around $\bar{b}$, the following expression can be written:

$$\bar{c} = \frac{\bar{a}}{\bar{b}} \int \left(1 - \frac{\delta b}{\bar{b}} + \frac{\delta b^2}{\bar{b}^2} - \frac{\delta b^3}{\bar{b}^3} + \frac{\delta b^4}{\bar{b}^4} - \ldots\right) f_b(\delta b)\, d\delta b. \quad (A3)$$

In the previous integral, the coefficient linear in $1/\bar{b}$ vanishes by the definition of $\bar{b}$, and it will converge or not depending on the analytical properties of f_b, but even if the series turns out to be asymptotic and eventually diverges it can be used to approximate the integral provided that only a few series terms are added. With this in mind and since there is no easy way to estimate the skewness of the error distributions in the data, only the first nonzero term is used, yielding

$$\bar{c} = \frac{\bar{a}}{\bar{b}} \left(1 + \frac{\sigma_b^2}{\bar{b}^2}\right), \quad (A4)$$

which is the expression used.

[10] The expression used originates from $M = 3kG^{-1}R_e\sigma^2$, where the structural constant k varies with different galaxy surface density profiles. Since the surface brightness profile of LCBGs is consistent with an exponential law (Koo et al. 1994), we adopt $k = 1.7$, following Bender et al. (1992).

REFERENCES

Balzano, V. A. 1983, ApJ, 268, 602
Bender, R., Burstein, D., & Faber, S. M. 1992, ApJ, 399, 462
Bershady, M. A., et al. 2004, in preparation
Burstein, D., & Heiles, C. 1984, ApJS, 54, 33
Cowie, L. L., Songaila, A., & Hu, E. M. 1991, Nature, 354, 460
de Vaucouleurs, G., de Vaucouleurs, A., Corwin, H. G., Jr., Buta, R. J., Paturel, G., & Fouqué, P. 1991, Third Reference Catalogue of Bright Galaxies (New York: Springer)
Díaz, A. I. 1998, Ap&SS, 263, 143
González-Delgado, R. M., Pérez, E., Díaz, A. I., García-Vargas, M. L., Terlevich, E., & Vilchez, J. M. 1995, ApJ, 439, 604
Guzmán, R., Gallego, J., Koo, D. C., Phillips, A. C., Lowenthal, J. D., Faber, S. M., Illingworth, G. D., & Vogt, N. P. 1997, ApJ, 489, 559
Guzmán, R., Jangren, A., Koo, D. C., Bershady, M. A., & Simard, L. 1998, ApJ, 495, L13
Guzmán, R., Koo, D. C., Faber, S. M., Illingworth, G. D., Takamiya, M., Kron, R. G., & Bershady, M. A. 1996, ApJ, 460, L5
Hoyos, C. 2002, master's thesis, Univ. Autónoma de Madrid
Hoyos, C., & Díaz, A. I. 2004, in preparation
Im, M., Ratnatunga, K. U., Griffiths, R. E., & Casertano, S. 1995, ApJ, 445, L15
Jangren, A., Bershady, M. A., Conselice, C., Koo, D. C., & Guzmán, R. 2004, AJ, submitted
Kennicutt, R. C., Jr. 1983, ApJ, 272, 54
Kennicutt, R. C., Jr., Tamblyn, P., & Congdon, C. E. 1994, ApJ, 435, 22
Kobulnicky, H. A., & Zaritsky, D. 1999, ApJ, 511, 118
Koo, D. C., Bershady, M. A., Wirth, G. D., Stanford, S. A., & Majewski, S. R. 1994, ApJ, 427, L9
Koo, D. C., Guzmán, R., Faber, S. M., Illingworth, G. D., Bershady, M. A., Kron, R. G., & Takamiya, M. 1995, ApJ, 440, L49
Lehnert, M. D., & Heckman, T. M. 1996, ApJ, 472, 546
Lilly, S. J., Tresse, L., Hammer, F., Crampton, D., & Le Fevre, O. 1995, ApJ, 455, 108
Lowenthal, J. D., et al. 1997, ApJ, 481, 673
Noeske, K. G., Guseva, N. G., Fricke, K. J., Izotov, Y. I., Papaderos, P., & Thuan, T. X. 2000, A&A, 361, 33
Osterbrock, D. E. 1989, Astrophysics of Gaseous Nebulae and Active Galactic Nuclei (Mill Valley: University Science Books)
Pagel, B. E. J., Edmunds, M. G., Blackwell, D. E., Chun, M. S., & Smith, G. 1979, MNRAS, 189, 95
Pettini, M., Kellogg, M., Steidel, C. C., Dickinson, M., Adelberger, K. L., & Giavalisco, M. 1998, ApJ, 508, 539
Phillips, A. C., Guzmán, R., Gallego, J., Koo, D. C., Lowenthal, J. D., Vogt, N. P., Faber, S. M., & Illingworth, G. D. 1997, ApJ, 489, 543
Sandage, A., & Tammann, G. 1974, ApJ, 190, 525
Sargent, W. L. W., & Searle, L. 1970, ApJ, 162, L155
Schaerer, D. 2002, in Star Formation and the Physics of Young Stars, ed. J. Bouvier & J.-P. Zahn (EAS Publications Series, Vol. 3) (Les Ulis: EDP Sciences), 53
Telles, E., Melnick, J., & Terlevich, R. 1997, MNRAS, 288, 78
Terlevich, R., Melnick, J., Masegosa, J., Moles, M., & Copetti, M. V. F. 1991, A&AS, 91, 285
Tresse, L., Rola, C., Hammer, F., Stasińska, G., Le Fèvre, O., Lilly, S. J., & Crampton, D. 1996, MNRAS, 281, 847
Whitford, A. E. 1958, AJ, 63, 201
Zwicky, F. 1965, ApJ, 142, 1293